AGU PUBLICATIONS

Geophysical Research Letters

RESEARCH LETTER

10.1002/2015GL067034

**Key Points:**

- The spatial biases of back projections are caused by slowness errors
- The slowness errors can be calibrated by travel time corrections of aftershocks
- The 2015 Gorkha earthquake is a deep and incomplete Himalayan rupture

**Supporting Information:**

- Figures S1–S3 and Table S1

**Correspondence to:**
L. Meng,
meng@ess.ucla.edu

**Citation:**
Meng, L., A. Zhang, and Y. Yagi (2016), Improving back projection imaging with a novel physics-based aftershock calibration approach: A case study of the 2015 Gorkha earthquake, *Geophys. Res. Lett.*, *43*, 628–636, doi:10.1002/2015GL067034.

Received 16 NOV 2015
Accepted 3 JAN 2016
Accepted article online 6 JAN 2016
Published online 22 JAN 2016

# Improving back projection imaging with a novel physics-based aftershock calibration approach: A case study of the 2015 Gorkha earthquake

**Lingsen Meng[1], Ailin Zhang[1], and Yuji Yagi[2]**

[1]Earth, Planetary, and Space Sciences, University of California, Los Angeles, California, USA, [2]Department of Earth Evolution Sciences, Tsukuba, Japan

**Abstract** The 2015 $M_w$ 7.8 Nepal-Gorkha earthquake with casualties of over 9000 people was the most devastating disaster to strike Nepal since the 1934 Nepal-Bihar earthquake. Its rupture process was imaged by teleseismic back projections (BP) of seismograms recorded by three, large regional networks in Australia, North America, and Europe. The source images of all three arrays reveal a unilateral eastward rupture; however, the propagation directions and speeds differ significantly between the arrays. To understand the spatial uncertainties of the BP analyses, we analyze four moderate size aftershocks recorded by all three arrays exactly as had been conducted for the main shock. The apparent source locations inferred from BPs are systematically biased from the catalog locations, as a result of a slowness error caused by three-dimensional Earth structures. We introduce a physics-based slowness correction that successfully mitigates the source location discrepancies among the arrays. Our calibrated BPs are found to be mutually consistent and reveal a unilateral rupture propagating eastward at a speed of 2.7 km/s, localized in a relatively narrow and deep swath along the downdip edge of the locked Himalayan thrust zone. We find that the 2015 Gorkha earthquake was a localized rupture that failed to break the entire Himalayan décollement to the surface, which can be regarded as an intermediate event during the interseismic period of larger Himalayan ruptures that break the whole seismogenic zone width. Thus, our physics-based slowness correction is an important technical improvement of BP, mitigating spatial uncertainties and improving the robustness of single and multiarray studies.

## 1. Introduction

As an emerging tool for earthquake source imaging, the back projection (BP) approach has been effective for imaging the complexity of the dynamic rupture of large earthquakes. It has provided robust views of the recent large earthquakes, such as the 2010 Chilean earthquake [*Kiser and Ishii* 2011; *Koper et al.*, 2012], the 2011 Tohoku-Oki earthquake [*Meng et al.*, 2011; *Zhang et al.*, 2011], the 2012 off-Sumatra earthquake [*Meng et al.*, 2012; *Satriano et al.*, 2012; *Wang et al.*, 2012] and the 2014 Iquique Earthquake [*Meng et al.*, 2015; *Schurr et al.*, 2014]. BP constrains the spatiotemporal properties of the rupture (length, direction, speed, and segmentation) based solely on the phase of coherent seismic array signals. Thus, it can be characterized as a "stochastic" approach, as it does not rely on detailed knowledge of Green's functions, on restrictive parameterizations of the rupture kinematics, nor on additional smoothing. Because it captures high frequency seismic radiation, BP is capable of revealing fine details of the rupture process and is a crucial tool to discriminate among complicated physical models in theoretical earthquake source studies.

BP is based upon a simple principle for tracking a moving target, similar to those that use antennae to locate and track sources of motion in military and civilian applications [*Rost and Thomas*, 2002]. During large earthquakes, strong seismic waves are typically assumed to radiate from the rupture front. Tracking the source of the seismic waves during such events depicts the course of the rupture front. While standard seismic array processing techniques calculate the travel times based on one-dimensional reference velocity models, BP offers superior resolution because it also takes into account the travel time variations due to three-dimensional Earth structure. This travel time variation is accounted for using a procedure referred to as the "hypocenter correction." BP aligns the waveforms of the initial arrival of *P* waves, which are assumed to originate from the hypocenter. The subsequent ruptures are tracked based on their differential travel times relative to the hypocenter, similar to the concept of "relative earthquake relocation method" [e.g. *Lees*, 1998]. Additional array processing techniques, such as nonlinear stacking [*Koper et al.*, 2011], multiple signal classification (MUSIC) method [*Meng et al.*, 2011], and compressive sensing [*Yao et al.*, 2011] have been introduced with the intent to further improve the resolution of BP. But the timing correction at the hypocenter remains the key element providing high resolution imaging, since it was introduced by *Ishii et al*. [2005] for the 2004 Sumatra earthquake.

However, BP has been shown to have significant limitations. The hypocenter correction presumes uniform travel time errors across the entire rupture area, even at large distance from the hypocenter. While it is valid at the vicinity of the hypocenter, in the case of large, finite ruptures, the correction becomes increasingly less accurate as the rupture front moves away from the hypocenter. Further, since the travel time error is a function of seismic raypath, the resulting spatial bias in BP differs between various arrays. Thus, the hypocenter correction merits improvement in order to mitigate the spatial uncertainty of BP and the discrepancies between different arrays. *Ishii et al*. [2007] addressed this problem by calibrating the location-dependent travel time errors using the aftershocks of the 2004 Sumatra earthquake. The study obtained travel time corrections at each aftershock location by cross correlating the aftershock waveforms and then interpolating the time correction at a grid point of the fault plane. The corrections were then applied to images of the main shock rupture.

While the technique provided a new strategy, it also had practical limitations. It depends upon the presence of aftershocks larger than M5.5 to have sufficient signal-to-noise ratio at teleseismic distance. In fact, such aftershocks tend to be sparse and typically distributed at the fringes rather than inside the large coseismic rupture. Thus, the strategy is limited by the use of empirical interpolation, which requires uniform and dense distribution of the calibration aftershocks. Further, the empirically calibrated BP method shows incoherent energy around the aftershocks, suggesting that the strategy introduces artifacts in the main shock BP [*Ishii et al*., 2007]. To overcome these issues, a physics-based approach is necessary to improve aftershock calibration in BP imaging.

The 2015 $M_w$ 7.8 Nepal-Gorkha earthquake provides a useful test case for understanding and mitigating the spatial bias of BP. With casualties of over 9000 people, it was the most devastating disaster to strike Nepal since the 1934 Nepal–Bihar earthquake. The rupture process of the earthquake, which is rarely recorded by more than two arrays for typical large global earthquakes, was well captured by BP at three continental arrays within teleseismic distances from the Gorkha earthquake. Multiple source studies of the Gorkha earthquake show eastward directivity [*Avouac et al*., 2015; *Fan and Shearer* 2015; *Galetzka et al*., 2015; *Yagi and Okuwaki*, 2015]. However, the detailed rupture pattern differs between the BP studies. In our previous work, we find that BP of the Australian network shows an almost linear rupture pattern, consistent with a narrow slip distribution [*Avouac et al*., 2015]. In contrast, the BP images from global stations show much more complicated rupture patterns, indicating multiple stages and involving broader along-dip slip distribution [*Fan and Shearer*, 2015; *Yagi and Okuwaki*, 2015]. To understand and resolve the discrepancies between these studies, we developed a physics-based calibration approach that enhances the spatial accuracy of BP.

In this study, we first image the Gorkha earthquake with three large arrays at different azimuth from the source region. Our results show that the propagating directions and the inferred rupture speeds differ significantly among the three arrays. By imaging aftershocks based on the hypocenter correction of the main shock, we find that the apparent source locations inferred from BP are systematically biased toward the receiver array. This bias can be explained by the uncertainty of the ray parameter (slowness) caused by approximating the three-dimensional velocity structures with a one-dimensional model. We develop a physics-based aftershock calibration by introducing an “error” in the slowness term that translates source locations of earthquakes into travel time. We find that with the slowness calibration, the BPs of three arrays are mutually consistent and reveal a simple pattern of unilateral rupture along the downdip edge of the locked Himalayan thrust zone. We conclude that our physics-based slowness correction enhances BP imaging by mitigating location bias.

## 2. Spatial Bias in Back Projections of the Gorkha Earthquake

The coseismic rupture process of the 2015 $M_w$ 7.8 Gorkha earthquake is imaged by BP, which provided a high frequency (HF) view of the rupture process. We use the seismograms recorded by the Australian seismic network (AU), the North America network (NA), and the European seismic network (EU), located at different azimuths from the source region (Figure 1b). The data are available from the Incorporated Research Institutions

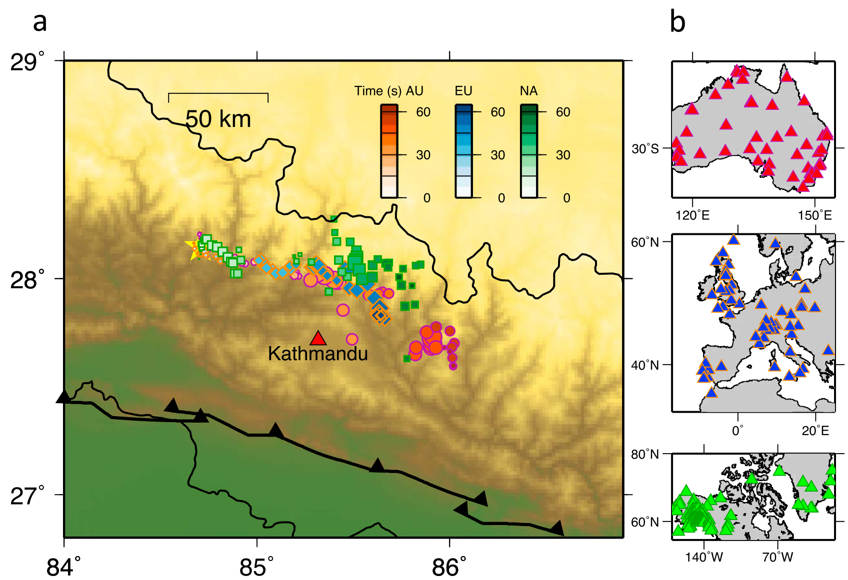


**Figure 1.** (a) Rupture process imaged from back projection by multiple arrays. The colored symbols, green squares, blue diamonds, and red circles show the spatial distribution of the high frequency radiation imaged by North America (NA), European (EU), and Australian (AU) array, respectively. The three colored bars denote the timing of high frequency radiations imaged by each array. (b) Station distributions of each array.

for Seismology (IRIS) data center (http://www.iris.edu). We filtered the seismograms between 0.5 s and 2 s, the highest band with relatively high waveform coherency (Figure S1 in the supporting information). We aligned the initial *P* wave arrivals of the filtered waveforms with a multichannel cross-correlation technique. The first arrival is assumed to come from the U.S. Geological Survey hypocenter location (84.71°E, 28.15°N). The location of the later HF sources is determined based on the differential travel time relative to the hypocenter. Since differential travel time is not sensitive to relatively small source depth changes along the shallow dipping Main Himalayan Thrust (MHT), we back projected the waveforms onto a horizontal fault plane at a depth of 15 km based on the IASP91 velocity model. We adopted the Multitaper-MUSIC array processing technique, which resolves more closely spaced sources and is less sensitive to aliasing, yielding a sharper image of the rupture process than the standard beamforming approach [*Meng et al*., 2011]. We also applied a "reference window" strategy [*Meng et al*., 2012], which eliminates the "swimming" artifacts of typical BPs, a systematic apparent drift of the HF energy toward the array.

Figure 1a shows that BP imaging of all three arrays indicates unilateral linear eastward rupture propagation. However, the rupture directions and the inferred rupture speeds differ significantly between each of the arrays. Several systematic differences are present: the apparent rupture length is shorter in the EU results (~90 km) than in the AU results (~150 km), leading to significantly different inferred rupture speeds (2.2 km/s and 2.8 km/s, respectively), and the apparent rupture direction is roughly east in the NA results but close to the 120° strike of the MHT in the EU and AU results.

To understand the array discrepancies and spatial uncertainties of the BP analyses, we imaged four significant aftershocks and compared the BP-inferred aftershock location with the location from the standard earthquake catalogs. We applied the "hypocenter correction" of the main shock to the aftershocks. This procedure is similar to the continuous BP where the BP is used as an approach to detect missing aftershocks [*Kiser and Ishii*, 2013]. We chose four moderate size (M5.5 ~ 6.7) aftershocks listed in Table S1. These aftershocks are large enough that there is sufficient energy in the high frequency band (~1 Hz). However, they are not so large that the centroid location of their ruptures cannot be considered collocated with the epicenter location in the earthquake catalog (i.e., the spatial extent of their ruptures is small). We then back projected the aftershocks recorded by all three arrays in the same fashion as the main shock. We averaged the BP locations of the first 5 s of the aftershocks and then compared them with the locations in standard earthquake catalogs issued by National Earthquake Information Center (NEIC), International Seismological Center (ISC), and Nepal National Seismological Center (NSC). We were interested in comparing the *relative* location of the aftershocks from the

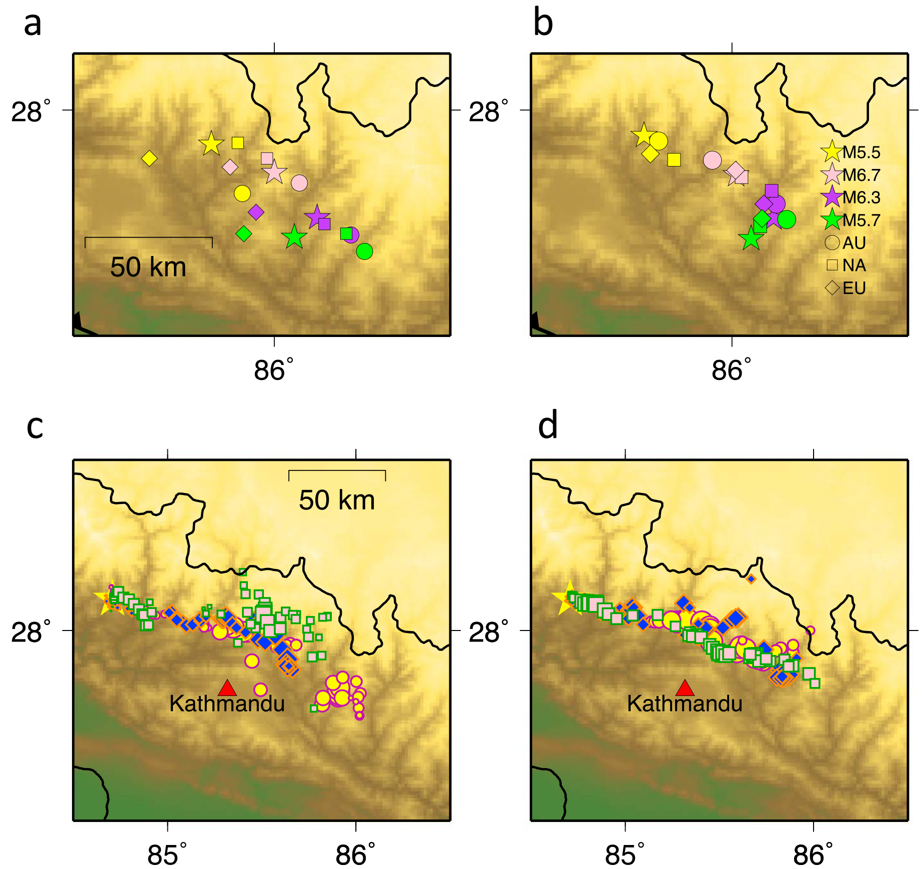


**Figure 2.** The back projections with slowness correction. (a and b) Aftershock locations inferred from back projection with catalog location before (a) and after (b) slowness correction. The stars show NEIC catalog locations of four moderate size (M5 ~ 7) aftershocks, with colors corresponding to four aftershocks. The symbols (circle, square, and diamond) denote apparent back projection locations imaged by the AU, NA, and EU arrays. (c and d) The main shock back projections of different arrays before (c) and after (d) correction.

main shock hypocenter. The various catalogs showed systematic bias in the locations of the earthquakes, but after adjusting for the systematic differences between earthquake catalogs, the catalog locations of the same aftershock turned out to be less than 5 km from each other, a relatively small discrepancy compared to the spatial bias of BP (on the order of 30 km). We found that the apparent source locations inferred from BP differ from the standard catalog locations and are systematically biased toward the array. Such differences occur because the resolution of BP is not isotropic; the resolution of the imaging is better in directions perpendicular to the raypath, rather than along the raypath where more significant distortions occur. (This is similar to differential resolution of azimuth and slowness in conventional seismic array processing.) Figure 2a shows that the spatial bias of each aftershock is generally, though not rigidly, along direction of the receiver.

## 3. Introducing a Physics-Based Aftershock Calibration

To introduce our slowness correction, we begin with the travel time calculation used in conventional BP. As the timing calculation in BP is similar in various array processing techniques (e.g., beamforming, MUSIC, and compressive sensing), we present a review of beamforming BP, which has a simple equation:

$$\mathrm{BP}(\xi, t) = \sum_j u_j\left(t + T_j^0(\xi)\right), \tag{1}$$

where $\mathrm{BP}(\xi, t)$ is the beamforming amplitude as a function of source location $\xi$ and time $t$, $T_j^0(\xi)$ is the travel time from source location $\xi$ to receiver station $j$, and the absolute travel time $T_j^0(\xi)$ can be described by the sum of the theoretical travel time $T_j^{\mathrm{cal}}(\xi)$ and the travel time error $\delta T_j(\xi)$. This error term $\delta T_j(\xi)$ is a timing

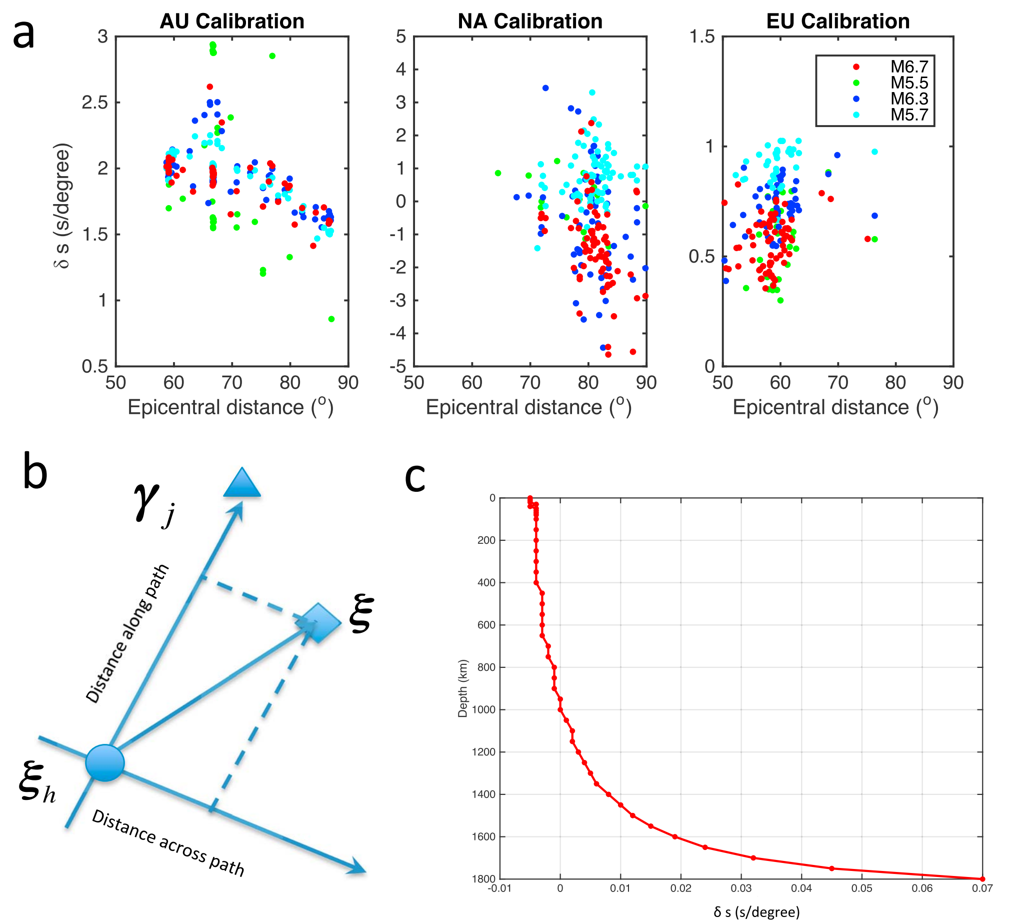


**Figure 3.** (a) Slowness error inferred from the aftershock calibrations. The three panels show the slowness error calibration for AU, NA, and EU arrays. In each panel, the colored dots denote the slowness error inferred from different events as a function of epicentral distance. (b) Illustration of differential travel time between two sources $\xi$ and $\xi_h$ under the far-field approximation in equation (4). (c) The effect of velocity uncertainty on the apparent slowness of direct *P* wave (ray parameters *p*). The curve shows the change of the apparent slowness $\delta s$ (ray parameters) as a function of a gaussian velocity perturbation with of a peak value of 0.5 km/s at different depth of the one-dimensional lasp91 model. The apparent slowness $\delta s$ is evaluated at epicentral distance of 75°, calculated with the Taup toolkit.

correction that accounts for the effect of the three-dimensional Earth structures. This correction was introduced in the initial BP study of the 2004 M9.2 Sumatra earthquake [*Ishii et al.*, 2005].

$$T_j^0(\xi) = T_j^{\mathrm{cal}}(\xi) + \delta T_j(\xi). \tag{2}$$

If one assumes variation of the travel time error $\delta T_j(\xi)$ is weakly dependent on the source location $\xi$, $\delta T_j(\xi)$ can be approximated by $\delta T_j(\xi)$, which is the travel time error derived at the hypocenter, and can be obtained by cross correlating the initial *P* waveforms ($\xi h$ stands for the hypocenter location).

$$\delta T_j(\xi) \simeq \delta T_j(\xi_h) = T_j^0(\xi_h) - T_j^{\mathrm{cal}}(\xi_h). \tag{3}$$

In theory, such approximation is valid only in the vicinity of the hypocenter. As the subsource moves away from the hypocenter, this correction becomes less effective. An additional correction is needed to account for the travel time error $\delta T_j(\xi)$ at a distant location $\xi$.

Based on the far-field approximation [*Aki and Richards*, 2002], one can obtain the differential travel time between two sources $\xi$ and $\xi h$ by multiplying the difference between their distances projected along the ray direction $\gamma_j$ with the slowness (Figure 3b).

$$T_j^{\mathrm{cal}}(\xi) \simeq T_j^{\mathrm{cal}}(\xi_h) + S_j\gamma_j \cdot (\xi - \xi_h), \tag{4}$$

where $\gamma_j$ is ray direction near the source and is the apparent slowness (ray parameter) evaluated from the hypocenter to the station *j*. This simplified equation suggests that the difference of source location across the raypath does not contribute to the differential travel time. In addition, the slowness controls the trade-off between source location and travel time. Since the bias of the main shock BP has a systematic orientation relative to the hypocenter, and the spatial discrepancies are larger when the source locations are farther away from the hypocenter, we hypothesize an error in , referred to as , could be responsible for the differential travel time error between a certain source location $\xi$ and the hypocenter $\xi_h$

$$\delta T_j(\xi) \simeq \delta T_j(\xi_h) + \delta s_j \gamma_j \cdot (\xi - \xi_h). \tag{5}$$

In practice, this slowness error term can be calculated from the difference between travel time errors at the hypocenter of the main shock $\xi_h$ and a given aftershock location $\xi$.

$$\delta s_j \simeq \left[\delta T_j(\xi_h) - \delta T_j(\xi)\right] / \left[\gamma_j \cdot (\xi - \xi_h)\right]. \tag{6}$$

We then used the bias of the aftershock location to infer the slowness errors for each of the AU, NA, and EU arrays based on equation (6). Figure 3a shows slowness errors as a function of epicentral distance. For the AU array, despite the scattering, a systematic trend in slowness exists as a function of epicentral distance, resulting in spatial errors in BP locations. The plot of the AU array also suggests that the negative slopes of slowness error, as a function of distance, bias the apparent source closer to the array. This correlation between slowness error and epicentral distance suggests that the path effect of the AU array is relatively uniform and can be potentially accounted by an alterative one-dimensional velocity model. The NA and EU arrays have larger scatters with no systematic trend in slowness errors as a function of epicentral distance, which demonstrate the complicated pattern of the slowness uncertainties due to three-dimensional Earth structure. Once the slowness is determined, we introduce a modified version of BP with the slowness corrections based on aftershocks (equation (7)).

$$\mathrm{BP}(\xi, t) = \sum_j u_j\Big(t + T_j^0(\xi_h) + \big(s_j + \delta s_j\big)\gamma_j \cdot (\xi - \xi_h)\Big). \tag{7}$$

The new equation includes a modification of the travel time correction due to slowness error , as described in equation (5). Note that depends only on the station j for a given source-array setting and is independent of the source parameterization. To obtain a characteristic slowness error for the aftershocks at a given station, we take the median slowness error of all available aftershocks recorded at that station. The slowness error is due to the difference between path effect of the one-dimensional velocity model and the three-dimensional Earth structure. Figure 3c shows the change of the apparent slowness (ray parameters) value as a function of depth with constant velocity perturbations. It clearly shows that the velocity uncertainty at greater depths leads to a larger slowness error. Each array shares the same shallow velocity structure right beneath the source, but as the seismic waves dive into the mantle toward the receiver array, they travel through different deep structure. Thus, the slowness errors, and consequently the BP biases, systematically differ between arrays.

Figures 2b and 2d show the calibrated BPs of the aftershocks and the main shock. The calibration based on our slowness correction significantly mitigates the spatial bias of BP. The BP-determined aftershock locations are in agreement with the catalog locations. The remaining differences between the catalog locations and locations estimated from arrays is on the order of 10 km and can be taken as a measure of the location uncertainties of BP. Once the slowness correction is applied to the main shock, BP results from the three arrays are also in better agreement with each other (Figure 2d). In contrast to the broad and complex energy distribution of prior BP studies using global stations [*Fan and Shearer*, 2015; *Yagi and Okuwaki*, 2015], the calibrated BP reveals a remarkably linear rupture pattern indicating narrow and concentrated HF radiation. We also produced a combined BP image of all three arrays by averaging the BP power images at each time snapshot. The combined BP shows a consistent linear trend, and the accumulated energy plot (Figure 4b) is also remarkably simple compared to the prior BP studies using a global network. Our results confirm the initial findings of *Avouac et al*. [2015], indicating that HF radiation was released along the west-to-east rupture spatially coincident with the downdip edge of the locked region of the MHT. Note that due to lack of the depth resolution of BP, this interpretation assumes that the coseismic rupture mainly occurred at the depth of the MHT. The spatial distribution of the HF sources is at the downdip boundary of the finite slip model (Figure 4a),

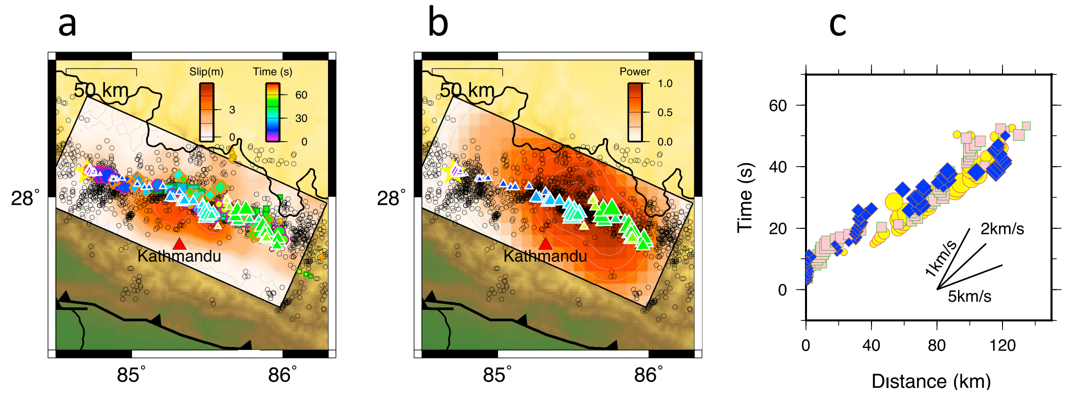


**Figure 4.** (a) Comparisons of back projection with finite fault model. The circle, square, and diamond denote the calibrated back projection locations imaged by the AU, NA, and EU arrays, respectively, color coded by time. The triangles with the white edges denote the merged back projection from all three arrays. The reddish color contours show the finite fault model based on joint inversion of seismic and geodetic data [*Avouac et al.*, 2015]. (b) Merged back projection (triangles with white edges) of three arrays with the accumulated beamforming energy in the red background contour map. (c) The rupture distance along strike of MHT as a function of time for the AU (yellow circles), NA (pink squares), and EU (blue diamond) arrays.

which is sensitive to the low frequency and static deformation field. In addition, we find that the rupture direction and speed from the three arrays are now consistent. The inferred rupture speed is 2.7 km/s, aligned with that derived in various finite source inversions [e.g., *Avouac et al.*, 2015; *Galetzka et al.*, 2015] (Figure 4c).

To further understand the effect of our slowness correction under more complicated and realistic circumstances, we conducted a kinematic rupture scenario involving a unilateral rupture trending along the strike of MHT over a length of 150 km (Figure S2). This scenario is inspired by our BP of the Gorkha earthquake. The rupture comprises six moving sources with a spatial interval of 30 km. This spacing is chosen so that the sources are dense enough to represent a continuous rupture, yet the coda wave maintains realistic decay of waveform coherency. The rupture times correspond to an assumed rupture speed of 3 km/s. To include key characteristics of the realistic wavefield, we used the waveforms of an M6.7 event, which occurred on 26 April 2015, as empirical Green's functions. We introduced our slowness error as derived in Figure 3a. We back projected the seismograms constructed for NA, AU, and EU arrays at periods from 0.5 s to 2 s with a window length of 10 s, the same processing strategy as used in the main shock BP. The BP results without the slowness correction reproduce the expected bias of rupture length and direction (Figure S2, left). After the correction, the BPs of all three arrays recover the HF radiators along the line of the rupture, almost exactly reproducing the input rupture scenario (Figure S2, right). The AU results are noisier and show larger scatters of the HF sources, possibly due to the relatively small slowness correction of the AU array and the notable finite rupture effect of the M6.7 earthquake. Overall, the synthetic test demonstrates that BP with our slowness correction is capable of imaging the input scenarios.

## 4. Summary and Discussion

In this study, we explain the origin of the location bias and array discrepancies in BP imaging at a consequence of a slowness error caused by the uncertainty of the one-dimensional reference velocity model. In the case study of the 2015 M7.8 Gorkha earthquake, we find that the spatial discrepancies of three large regional arrays are significant but can be effectively mitigated by introducing a physics-based slowness correction term. This correction term is calibrated using the location errors of the aftershocks. With the aftershock calibrations, the BPs of the multiple arrays are found to be in good agreement with each other. They reveal a narrow, unilateral rupture, propagating eastward at a speed of 2.7 km/s, spatially coincident with the downdip edge of the locked Himalayan thrust zone. The rupture extends over ~150 km, consistent with a confined slip distribution inferred from other source studies [*Avouac et al.*, 2015; *Galetzka et al.*, 2015].

In our case study of the 2015 Gorkha earthquake, the deep and localized rupture imaged by calibrated BP is consistent with the lack of surface ruptures found in geological surveys conducted after the event [*Angster et al.*, 2015]. In that sense, the Gorkha earthquake is a localized rupture that failed to penetrate the entire

Himalayan décollement to the surface, which appears similar to the 1833 earthquake [*Martin et al*., 2015]. A much larger rupture across the entire seismogenic depth, as large as M8.5, has been anticipated joining this and adjacent segments of the MHT, based on the geodetically observed high plate coupling and large slip deficit [*Ader et al*., 2012; *Bilham et al*., 2001]. One possible explanation for the localized rupture is that the updip and downdip segments along the Himalayan thrust may have been involved in events of different recurrent behaviors. In earthquake cycle simulations of large events driven by deep creep, small, frequent earthquakes are not uncommon [*Wu and Chen*, 2014]. The stress on the coupled zone tends to be nonuniform and larger near the deep edge of the locked zone. Thus, in the interseismic period between large and characteristic earthquakes, smaller earthquakes may nucleate near the deep edge without propagating into areas that are not yet sufficiently loaded by deep creep [*Wu and Chen*, 2014]. The downdip portion of the megathrust may involve more abundant but smaller events, with relatively short earthquake cycles. As the loading accumulates and the high-stress region grows over time, these smaller events will eventually lead to a rupture across the entire coupled width. These phenomena are also present in the Tohoku region, where M7 earthquakes occur in the downdip region on the average of every 30 years, while the M9 earthquake cycle in the updip region is on the order of 500 ~ 1000 years [*Uchida and Matsuzawa*, 2011].

The case study of the Gorkha earthquake demonstrates the importance of accounting for the slowness error in BP. The slowness error provides a physical framework to understand discrepancies between results from different arrays and offers an opportunity to mitigate this long-standing problem in BP imaging. In fact, the slowness correction is as important as the initial hypocenter correction, which provides the BP with its high resolution. Compared with the empirical calibration that requires dense and uniform distribution of aftershocks [e.g., *Ishii et al*., 2007], our physics-based calibrations can operate with a single aftershock and does not introduce artifacts of incoherent energy. Figure S3 shows the slowness calibration with a single aftershock (the M6.7 earthquake). Overall, we consider the single-aftershock calibration significant reduced the spatial biases in BP, although the complete calibration based on all four aftershocks delivers better consistency between arrays. The slowness correction improves the robustness of BP imaging and provides more reliable fine details of earthquake processes, such as the rupture speed, rupture segmentation, and spatial distribution of secondary sources. Ultimately, the correction may offer new opportunities to address important questions in earthquake source dynamics.

The slowness correction is also important for BP using global stations. The BP method was initially applied to recordings from large regional arrays. Recently, studies have begun exploring BP using globally distributed stations. Global BP has both advantages and disadvantages when compared with regional BP. The resolution of BP is proportional to the size of the array, so, ideally, global BP promises better resolution than regional BP. However, because the raypath passes through very different earth structures toward each station of a distributed global network, the waveform coherency and hence the quality of the BP imaging is relatively low compared to that of the regional array at high frequencies. Moreover, the variation between slowness errors will be more significant in a global network than those in a regional array, which have systematic errors caused by paths that share similar large-scale structures. Thus, without a slowness error calibration, global BP may not show consistent spatial bias as seen in BP of regional array. But the large variation of slowness error might result in less coherent energy and artificial rupture complexity, as seen in previous studies. In our future work, we will explore the slowness correction for BP using global stations, to revisit and revise the source images of large earthquakes, including those that occurred prior to the establishment of large regional arrays (e.g., USArray, and Hinet).

**Acknowledgments**
This research was supported by Hellman Fellowship and Knopoff foundation. The IRIS (www.iris.edu) and the European ORFEUS (www.orfeus-eu.org) data centers provided access to broadband seismograms. The earthquake catalogs are obtained from International Seismological Center (ISC) bulletin (http://www.isc.ac.uk/), National Earthquake Information Center (NEIC) (http://earthquake.usgs.gov/), and Nepal National Seismological Centre (NSC) (http://www.seismonepal.gov.np/). We thank Pablo Ampuero for valuable discussions about aftershock calibrations of BP and the implications on the rupture dynamics of the Gorkha earthquake. We thank the reviewers Gavin Hayes and Susan Hough for their very helpful comments and suggestions.

## References

Ader, T., et al. (2012), Convergence rate across the Nepal Himalaya and interseismic coupling on the Main Himalayan Thrust: Implications for seismic hazard, *J. Geophys. Res.*, *117*, B04403, doi:10.1029/2011JB009071.

Aki, K., and P. G. Richards (2002), *Quantitative Seismology*, vol. 1, Univ. Science Books, Sausalito, Calif.

Angster, S., E. J. Fielding, S. Wesnousky, I. Pierce, D. Chamlagain, D. Gautam, B. N. Upreti, Y. Kumahara, and T. Nakata (2015), Field reconnaissance after the 25 April 2015 M 7.8 Gorkha earthquake, *Seismol. Res. Let.*, *86*(6), 1506–1513.

Avouac, J.-P., L. Meng, S. Wei, T. Wang, and J.-P. Ampuero (2015), Lower edge of locked Main Himalayan Thrust unzipped by the 2015 Gorkha earthquake, *Nat. Geosci.*, *8*(9), 708–711, doi:10.1038/ngeo2518.

Bilham, R., V. K. Gaur, and P. Molnar (2001), Himalayan seismic hazard, *Science*(Washington), *293*(5534), 1442–1444.

Fan, W., and P. M. Shearer (2015), Detailed rupture imaging of the 25 April 2015 Nepal earthquake using teleseismic *P* waves, *Geophys. Res. Lett.*, *42*, 5744–5752, doi:10.1002/2015gl064587.

Galetzka, J., et al. (2015), Slip pulse and resonance of the Kathmandu basin during the 2015 Gorkha earthquake, Nepal, *Science*, *349*(6252), 1091–1095.

Ishii, M., P. M. Shearer, H. Houston, and J. E. Vidale (2005), Extent, duration and speed of the 2004 Sumatra–Andaman earthquake imaged by the Hi-Net array, *Nature*, *435*(7044), 933–936.

Ishii, M., P. M. Shearer, H. Houston, and J. E. Vidale (2007), Teleseismic *P* wave imaging of the 26 December 2004 Sumatra-Andaman and 28 March 2005 Sumatra earthquake ruptures using the Hi-net array, *J. Geophys. Res.*, *112*, B11307, doi:10.1029/2006JB004700.

Kiser, E., and M. Ishii (2011), The 2010 Mw 8.8 Chile earthquake: Triggering on multiple segments and frequency-dependent rupture behavior, *Geophys. Res. Lett.*, *38*, L07301, doi:10.1029/2011GL047140.

Kiser, E., and M. Ishii (2013), Hidden aftershocks of the 2011 Mw 9.0 Tohoku, Japan earthquake imaged with the backprojection method, *J. Geophys. Res. Solid Earth*, *118*, 5564–5576.

Koper, K. D., A. R. Hutko, T. Lay, C. J. Ammon, and H. Kanamori (2011), Frequency-dependent rupture process of the 2011 M w 9.0 Tohoku Earthquake: Comparison of short-period *P* wave backprojection images and broadband seismic rupture models, *Earth Planets Space*, *63*(7), 599–602.

Koper, K. D., A. R. Hutko, T. Lay, and O. Sufri (2012), Imaging short-period seismic radiation from the 27 February 2010 Chile (Mw 8.8) earthquake by back-projection of P, PP, and PKIKP waves, *J. Geophys. Res.*, *117*, B02308, doi:10.1029/2011JB008576.

Lees, J. M. (1998), Multiplet analysis at Coso geothermal, *Bull. Seismol. Soc. Am.*, *88*(5), 1127–1143.

Martin, S. S., S. E. Hough, and C. Hung (2015), Ground motions from the 2015 Mw7.8 Gorkha, Nepal, earthquake, constrained by a detailed assessment of macroseismic data, *Seismol. Res. Lett.*, *86*(6), 1524–1532.

Meng, L., J. P. Ampuero, J. Stock, Z. Duputel, Y. Luo, and V. C. Tsai (2012), Earthquake in a maze: Compressional rupture branching during the 2012 Mw 8.6 Sumatra earthquake, *Science*, *337*(6095), 724–726.

Meng, L., H. Huang, R. Bürgmann, J. P. Ampuero, and A. Strader (2015), Dual megathrust slip behaviors of the 2014 Iquique earthquake sequence, *Earth Planet. Sci. Lett.*, *411*, 177–187.

Meng, L., A. Inbal, and J. P. Ampuero (2011), A window into the complexity of the dynamic rupture of the 2011 Mw 9 Tohoku-Oki earthquake, *Geophys. Res. Lett.*, *38*, L00G07, doi:10.1029/2011GL048118.

Rost, S., and C. Thomas (2002), Array seismology: Methods and applications, *Rev. Geophys.*, *40*(3), 1008, doi:10.1029/2000RG000100.

Satriano, C., E. Kiraly, P. Bernard, and J. P. Vilotte (2012), The 2012 Mw 8.6 Sumatra earthquake: Evidence of westward sequential seismic ruptures associated to the reactivation of a N-S ocean fabric, *Geophys. Res. Lett.*, *39*, L15302, doi:10.1029/2012GL052387.

Schurr, B., et al. (2014), Gradual unlocking of plate boundary controlled initiation of the 2014 Iquique earthquake, *Nature*, *512*(7514), 299–302.

Uchida, N., and T. Matsuzawa (2011), Coupling coefficient, hierarchical structure, and earthquake cycle for the source area of the 2011 off the Pacific coast of Tohoku earthquake inferred from small repeating earthquake data, *Earth Planets Space*, *63*(7), 675–679, doi:10.5047/eps.2011.07.006.

Wang, D., J. Mori, and T. Uchide (2012), Supershear rupture on multiple faults for the $M_w$ 8.6 Off Northern Sumatra, Indonesia earthquake of April 11, 2012, *Geophys. Res. Lett.*, *39*, L21307, doi:10.1029/2012GL053622.

Wu, Y., and X. Chen (2014), The scale-dependent slip pattern for a uniform fault model obeying the rate-and state-dependent friction law, *J. Geophys. Res. Solid Earth*, *119*, 4890–4906.

Yagi, Y., and R. Okuwaki (2015), Integrated seismic source model of the 2015 Gorkha, Nepal, earthquake, *Geophys. Res. Lett.*, *42*, 6229–6235, doi:10.1002/2015GL064995.

Yao, H., P. Gerstoft, P. M. Shearer, and C. Mecklenbräuker (2011), Compressive sensing of the Tohoku-Oki Mw 9.0 earthquake: Frequency-dependent rupture modes, *Geophys. Res. Lett.*, *38*, L20310, doi:10.1029/2011GL049223.

Zhang, H., Z. Ge, and L. Ding (2011), Three sub-events composing the 2011 off the Pacific coast of Tohoku Earthquake (M w 9.0) inferred from rupture imaging by back-projecting teleseismic *P* waves, *Earth Planets Space*, *63*(7), 595–598.